Galindo, J.; Dolz, V.; García-Cuevas González, LM.; Ponce-Mora, A. (2020). Numerical evaluation of a solar-assisted jet-ejector refrigeration system: Screening of environmentally friendly refrigerants. Energy Conversion and Management. 210:112681-112681. https://doi.org/10.1016/j.enconman.2020.112681

# NUMERICAL EVALUATION OF A SOLAR-ASSISTED JET-EJECTOR REFRIGERATION SYSTEM: SCREENING OF ENVIRONMENTALLY FRIENDLY REFRIGERANTS

## Authors

José Galindo, Vicente Dolz [1], Luis Miguel García-Cuevas, Alberto Ponce-Mora

CMT – Motores Térmicos, Universitat Politècnica de València, Spain

## Abstract

The present paper evaluates numerically the feasibility of a solar jet-ejector refrigeration system from an efficiency maximization perspective with three low environmental impact refrigerants, namely, R1234yf, R1234ze and R600a. Special emphasis is given to the jet-ejector internal geometry optimization as a mechanism to improve the overall cycle performance. The jet-ejector entrainment ratio in different operating conditions and geometric configurations is determined by using a Computational Fluid Dynamics (CFD) approach experimentally validated which includes real gas models of R1234yf, R1234ze and R600a. R1234yf exhibited the best performance in terms of overall system efficiency closely followed by R600a and R1234ze. This suggests that the influence of the working fluid can be considerably mitigated if a thorough design of the jet-ejector is carried out. Afterwards, the refrigerant R1234yf is selected to carry out sensitivity studies with different collector typologies and solar irradiation scenarios. The Evacuated Tube Collector (ETC) model provided the highest overall system efficiency ($\eta_{ov} = 0.213$) for the peak solar irradiation (1000 $W/m^2$). Nevertheless, one of the Parabolic Trough Collectors (PTC)

[1] Corresponding Author: Vicente Dolz, CMT – Motores Térmicos, Universitat Politècnica de València, 46022, Spain. Email: vidolrui@mot.upv.es

models under investigation offered the most robust performance if a wider range of solar irradiation scenarios is considered.

## Keywords

Solar cooling, jet-ejector refrigeration, environmentally friendly refrigerants, energy efficiency, energy conversion, solar thermal collector

## Nomenclature

### Acronyms

| | |
|---|---|
| CFD | Computational Fluid Dynamics |
| COP | Coefficient Of Performance |
| GWP | Global Warming Potential |
| JERS | Jet-Ejector Refrigeration System |
| TMY | Typical Meteorological Year |

### Notation

### Latin

| | |
|---|---|
| $A$ | Area [m$^2$] |
| $c$ | Specific heat capacity [J/kg·K] |
| $k$ | Jet-ejector scaling factor [-] |
| $G$ | Solar irradiation [W/m$^2$] |
| $h$ | Specific enthalpy [J/kg] |
| $\dot{m}$ | Mass flow rate [kg/s] |
| $P$ | Pressure [bar] |
| $\dot{Q}$ | Heat exchanger power [W] |
| $T$ | Temperature [$°C$] |
| $\dot{W}$ | Mechanical power [W] |
| $Z$ | Compressibility factor [-] |

### Greek letters

| | |
|---|---|
| $\omega$ | Jet-ejector entrainment ratio [-] |

### Subscripts

| | |
|---|---|
| amb | Ambient |
| avg | Average |
| cl | Cooling load |
| co | Condenser |
| col | Solar collector |
| comp | Compressor |
| e | Jet-ejector |
| ev | Evaporator |

| | |
|---|---|
| ge | Generator |
| h | Hydraulic |
| in | Inlet |
| ind | Indoor |
| mf | Jet-ejector mixed flow |
| opt | Optimum |
| out | Outlet |
| ov | Overall system |
| pf | Jet-ejector primary flow |
| pm | Liquid pump |
| ref | Reference situation/condition |
| sat | Saturation |
| sf | Jet-ejector secondary flow |
| sol | Solar |
| t | Global solar irradiation |
| b,t | Direct solar irradiation |
| d,t | Diffuse solar irradiation |
| th | Thermal |

## 1. Introduction

Solar cooling technologies have received a great deal of interest in the last decades, especially in Mediterranean climates due to the peak electricity consumption of traditional refrigeration systems during summer periods. In fact, the energy consumption of refrigeration systems has been quantified around 40%-45% of the whole energy consumption in residential and commercial buildings [1,2].

Up to now, the limited market penetration of solar cooling systems can be ascribed to their high investment cost, a significant part of which is attributed to the solar collectors, the lack of practical knowledge and their control complexity due to the intermittent nature of solar irradiation [1,2]. Therefore, an efficiency increase in both the refrigeration cycle side and solar module side is crucial to improve the overall cycle performance and make these systems more attractive. Nevertheless, these technologies have great potential because, normally, the peak cooling demand is synchronized with the most favorable conditions to drive the solar cooling system (peak solar irradiation) [2,3]. Its implementation in warm climates could entail primary energy saving in the range of 40%-50% [1].

A vast amount of literature has been published concerning solar cooling applications with a predominance of absorption systems [4–6] and adsorption systems [7] due to their higher COP (ranging from 0.5-1.4 depending on the sorption machine configuration [8]). In comparison with sorption systems, jet-ejector

refrigeration systems show lower COP, however, they present lower installation cost and complexity [9,10]. Also, its versatility in terms of working fluid selection and its capability of integration with traditional refrigeration systems [11] are other positive aspects.

There are several research works available in the literature dealing with jet-ejector refrigeration cycles driven by solar energy following both a numerical and an experimental approach: Experimental facilities to determine the overall cycle performance [12,13], evaluation of the overall system behaviour over dynamic conditions [14,15], screening of different working fluids from a numerical perspective [16,17]. Research papers relative to jet-ejector single component are also common in literature from an experimental [18,19] and numerical perspectives (CFD) [20,21] with special focus on geometry design and evaluation of internal flow phenomena.

Research works dealing with jet-ejector solar cooling in which a thorough design of the jet-ejector internal geometry is done has rarely been performed in the literature. Recently, Bellos and Tzivanidis [10] conducted a numerical study of a solar assisted JERS in which the optimization is focused on a reduction of secondary flow pressure drop by using a 1D approach rather than an extensive optimization of its geometry. In addition, only one type of solar collector is examined and their investigation is not focused on environmentally friendly working fluids.

The main originality of the present paper is the feasibility evaluation of low ecological impact refrigerants (R1234yf, R1234ze, and R600a) on a solar-driven jet-ejector refrigeration system (JERS) with special emphasis on the design of the jet-ejector internal geometry. To maximize the jet-ejector performance, four key geometrical parameters are varied simultaneously together with the jet-ejector cycle generating temperature. Therefore, this work is intended to study the potential of a solar-driven JERS with further insight because the main development efforts are focused on the jet-ejector design. In addition, the influence of three kinds of solar collectors on the overall cycle performance is investigated.

The main objectives of the present paper can be summarized as follows:

- To conduct a computational evaluation of a solar-assisted jet-ejector refrigeration system working with environmentally friendly and new generation refrigerants, namely, R1234yf, R1234ze and R600a.

- To estimate the overall system efficiency, that is to say, the ratio between the incident solar radiation in different scenarios and the cooling capacity attained by the refrigeration cycle if the jet-ejector geometry is exhaustively optimized according to the reference operating conditions.
- To establish a close relationship between the jet-ejector cycle performance, the overall system performance, the solar collector side and the operating conditions.
- To carry out a sensitivity analysis to study the impact of different types of solar collectors over the overall system performance, specifically, Evacuated Tube Collectors (ETC), Compound Parabolic Concentrators (CPC) and Parabolic Trough Collectors (PTC).
- To compare the potential energy saving of the JERS with a traditional vapor-compression refrigeration system operating under the same cooling requirements and condensing temperature.

## 2. Solar refrigeration system description

The sketch of the JERS under investigation is shown in Figure 1 together with the solar collector field. The JERS is intended for air-conditioning applications and can be divided into two loops: On the refrigeration loop, the low-pressure secondary flow generates the desired cooling capacity as it evaporates in a heat exchanger. On the power loop, the high-pressure primary flow evaporates as it receives thermal energy coming from the low-grade heat source (solar collector field in this particular application) and expands within the jet-ejector thereby enabling suction of secondary flow inside the jet-ejector. Once the mixing and recompression processes are completed inside the jet-ejector, the resulting mixed-flow condenses in a heat exchanger rejecting heat to the environment in an intermediate pressure. Downstream the condenser a fraction of the liquid is recirculated to feed the pump of the power loop and the remainder is expanded trough the throttling valve to complete the refrigeration loop.

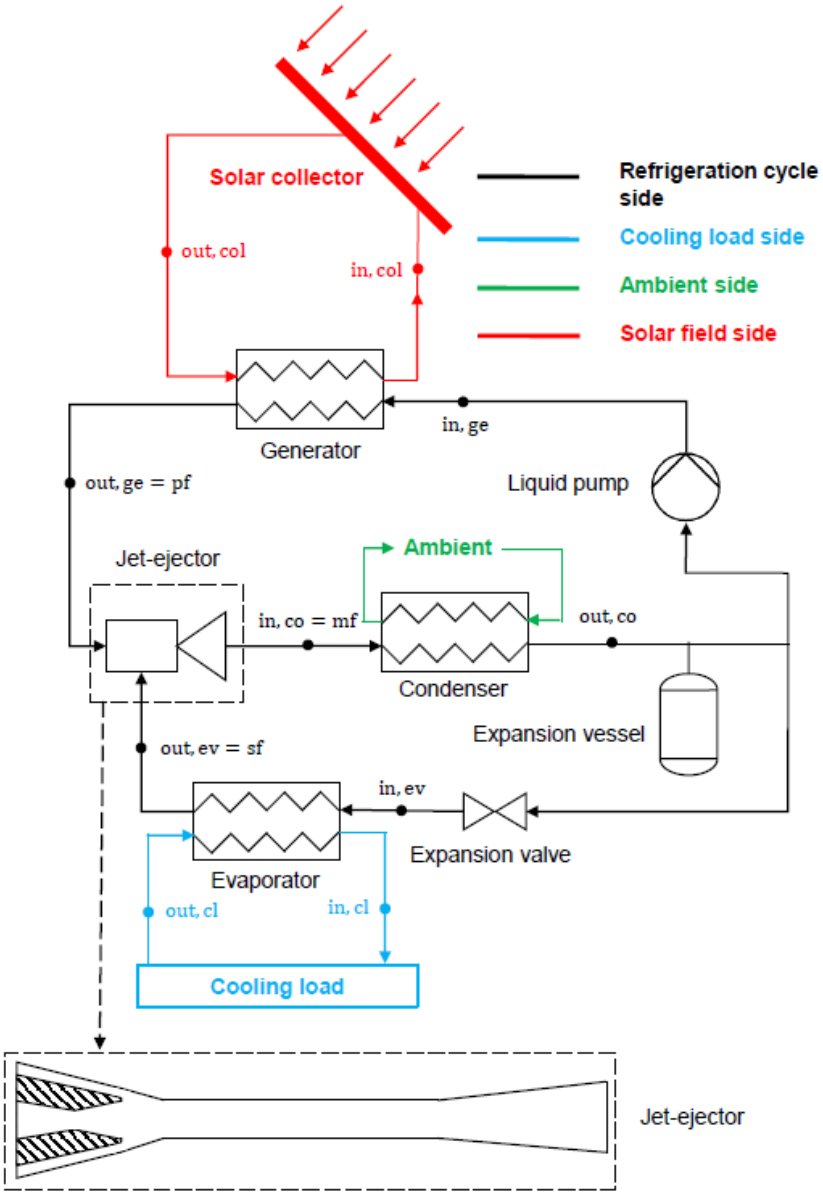


*Figure 1. Solar-assisted JERS and collector field layout*

The performance of both the JERS and the solar collector side can be defined by using power efficiency transformation from solar irradiation to thermal power and thermal power to cooling capacity:

$$\eta_{\mathrm{th-sol}} = \frac{\dot{Q}_{\mathrm{ge}}}{G_t \cdot A_{col}} \tag{1}$$

$$\eta_{\mathrm{th-cool}} = \frac{\dot{Q}_{\mathrm{ev}}}{\dot{Q}_{\mathrm{ge}}} = COP_{\mathrm{th}} \tag{2}$$

With the aim of simplifying the analysis, the JERS has been dimensioned for a rated thermal power ($\dot{Q}_{\mathrm{ge}}$) of 10 kW.

Likewise, the efficiency of the thermally-driven refrigeration cycle can be expressed as a function of the jet-ejector entrainment ratio and the specific enthalpy change occurring in the evaporator and the generator.

$$COP_{\mathrm{th}} = \frac{\dot{m}_{\mathrm{sf}} \cdot (h_{\mathrm{out,ev}} - h_{\mathrm{in,ev}})}{\dot{m}_{\mathrm{pf}} \cdot (h_{\mathrm{out,ge}} - h_{\mathrm{in,ge}})} = \omega \cdot \frac{h_{\mathrm{out,ev}} - h_{\mathrm{in,ev}}}{h_{\mathrm{out,ge}} - h_{\mathrm{in,ge}}} \quad (3)$$

Where $\omega$ refers to the jet-ejector entrainment ratio:

$$\omega = \frac{\dot{m}_{\mathrm{sf}}}{\dot{m}_{\mathrm{pf}}} \quad (4)$$

Then, the overall system efficiency governing the conversion of solar irradiation to cooling power is summarized in Equation (5):

$$\eta_{\mathrm{ov}} = \eta_{\mathrm{th-cool}} \cdot \eta_{\mathrm{th-sol}} = \frac{\dot{Q}_{\mathrm{ev}}}{G_{\mathrm{t}} \cdot A_{col}} \quad (5)$$

Where $G_{\mathrm{t}}$ is the incident global solar irradiation. To reduce the operative cost of the overall system both $\eta_{\mathrm{th-cool}}$ and $\eta_{\mathrm{th-sol}}$ must be maximized.

## 3. Solar refrigeration system operating conditions

This section is devoted to present the operating parameters and boundary conditions of the solar refrigeration system discriminating between the degrees of freedom (variables) and fixed parameters of both the solar field side and the JERS side.

On the solar field side, the solar irradiance data (global, direct and diffuse radiation) coming from satellite observations is presented. In addition, all the solar collector typologies under investigation are introduced as well as the main hypothesis adopted.

On the JERS side, in the first instance, a discussion of the working fluid selection is conducted. Subsequently, the cooling requirements and the outdoor conditions are defined thus fixing the condensing and evaporating temperatures of the JERS. Accordingly, the evaporating and condensing pressures can be determined for each refrigerant as well. Lastly, the jet-ejector internal geometry is described pointing out which geometric parameters are deemed as fixed or variable in the optimization process.

## 3.1 Solar field side

### 3.1.1 Solar irradiation level

Figure 2 shows the global solar irradiation over the area of Valencia Airport ($\text{latitude} = 39.489°, \text{longitude} = 0.478°$) for the typical meteorological year (computed in the time period 2006-2015). It provides information about the global solar irradiation distribution in the months with air-conditioning utilization (typically April-September). Figure 3 shows the hourly distribution of global solar radiation and ambient temperature over the same area for every day in the reference month of July (July 2014 in the TMY). As can be observed in Figure 3, some days the sky is partially cloudy, however, the hourly evolution of global solar irradiation follows a similar pattern. The collected dataset of daily surface irradiance parameters come from hourly measurements of geostationary Meteosat satellites. The solar radiation products are defined in the present paper for a particular geographical area, nevertheless, the irradiation pattern would be comparable in other Mediterranean latitudes.

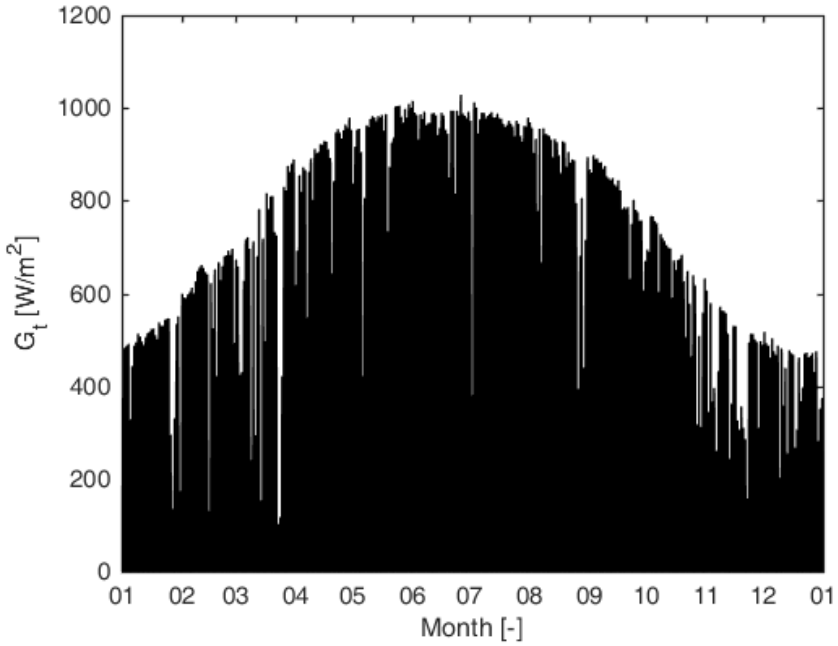


157

158 *Figure 2. Evolution of global solar irradiation along the typical meteorological year (TMY) in Valencia*

159 *Airport. Source: Photovoltaic Geographical Information Systems (PVGIS)* [22]

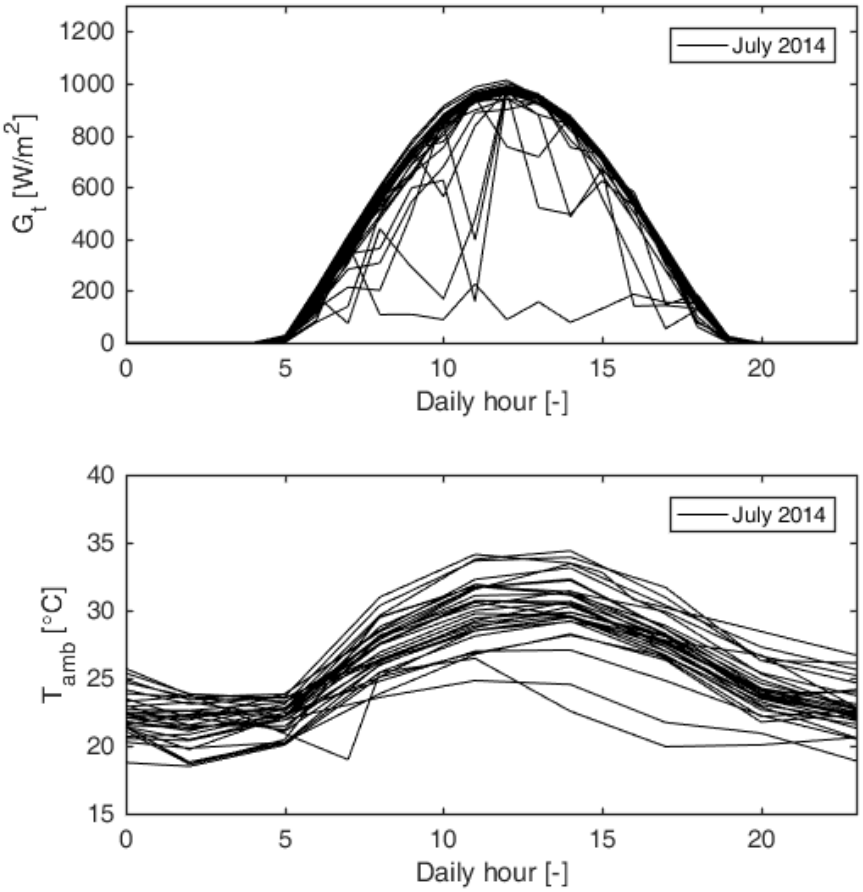


160

161 *Figure 3. Superposition of instantaneous daily global solar irradiation in Valencia Airport (July 2014)* [22]

162 *and daily evolution of the ambient temperature.*

163 Figure 4 depicts the global and direct solar irradiation of three sample days of July 2014 with clear sky

164 conditions. With this sample selection, the ratio between the diffuse and direct solar can be computed in

165 a favorable scenario. Thanks to meteorological data it is possible to make a realistic prediction of direct

166 $(G_{\mathrm{b,t}}/G_{\mathrm{t}})$ and diffuse $(G_{\mathrm{d,t}}/G_{\mathrm{t}})$ solar intensity ratios.

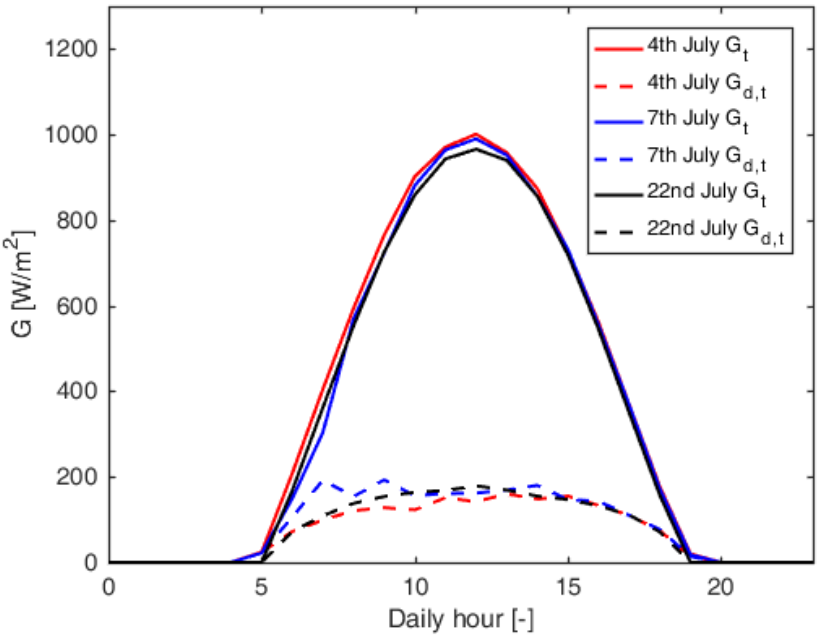


*Figure 4. Global and diffuse solar irradiation on three sample days with a clear sky scenario (July 2014). Source:* [22].

Table 1 shows four representative cases from Figure 4 which covers the time interval when the peak ambient temperature and the peak cooling demand normally occur. These meteorological parameters are used in the subsequent sensitivity analysis to feed the collector models in order to determine $\eta_{\mathrm{th-sol}}$.

| Case | Daily hour | $G_{\mathrm{t}}[\mathrm{W/m^2}]$ | $G_{\mathrm{d,t}}/G_{\mathrm{t}}[-]$ |
|---|---|---|---|
| C1 | ~11:30-12:30 | 1000 | 0.18 |
| C2 | ~10:00-11:00 & ~14:00-15:00 | 850 | 0.19 |
| C3 | ~09:00-10:00 & ~15:00-16:00 | 700 | 0.21 |
| C4 | ~08:00 & ~ 17:00 or Partially cloudy sky | 450 | 0.25 |

*Table 1. Four characteristic cases under evaluation*

### 3.1.2 Solar collector typology

Regarding the solar module classification, Flat Plate Collectors (FPC) have been used predominantly in available research works dealing with solar cooling systems, followed by Evacuated Tube Collectors (ETC) and, to a lesser extent, Compound Parabolic Concentrators (CPC) and Parabolic Trough Collectors (PTC)

[8,10]. The operating temperature of the solar collector is directly related to the collector type and design and high variability in collector operating temperature exists, even within the same collector's category. In the present paper a total amount of five solar collectors have been assessed: three PTC, one ETC and one CPC, (see Figure 5) and a certain representative value of collector outlet temperature has been selected for all of them: $T_{\text{out,col}} = 150°\text{C}$ [23]. Flat Plate Collectors have been disregarded because their maximum achievable temperature is normally limited to $\sim 90°\text{C}$ [24]. As will be discussed later the optimum driving temperature of the JERS considering some degree of vapor superheating is above this temperature.

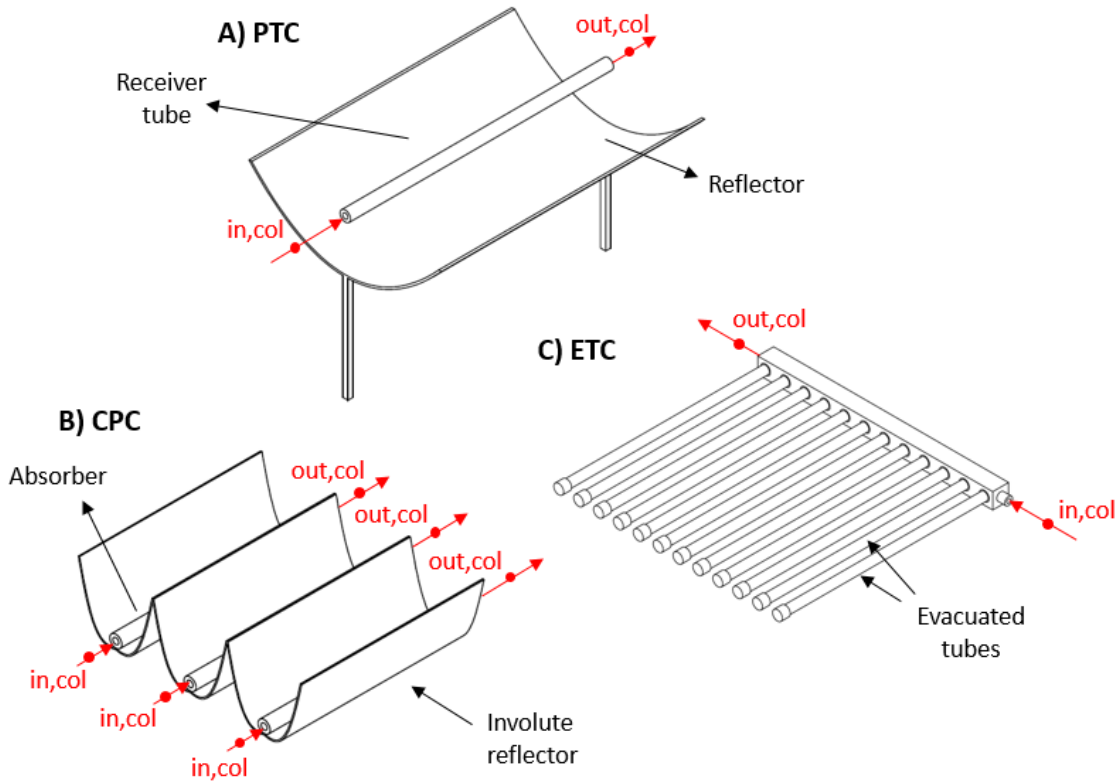


*Figure 5. Schematic view of the solar collectors under evaluation: A) Parabolic Trough Collector (PTC), B) Compound Parabolic Concentrator (CPC), C) Evacuated Tube Collector (ETC)*

## 3.2 Jet-ejector refrigeration system (JERS)

### 3.2.1 Working fluid

The system performance has been evaluated considering environmentally friendly working fluids to meet the increasingly stringent regulations, specifically, R1234yf, R1234ze and R600a. The Ozone Depletion Potential (ODP) of all the refrigerants under consideration is zero while their Global Warming Potential is very low (R1234yf, GWP = 4; R1234ze, GWP = 6; R600a, GWP=3). All of them have been considered before in solar cooling applications [16,18].

### 3.2.2 Jet-ejector internal geometry

The internal geometry of the jet-ejector strongly affects the expansion, entrainment and mixing processes and it must be carefully designed to maximize the JERS performance for given operating conditions. Figure 6 shows a schematic representation of the jet-ejector internal geometry and Table 2 provides its most relevant dimensions.

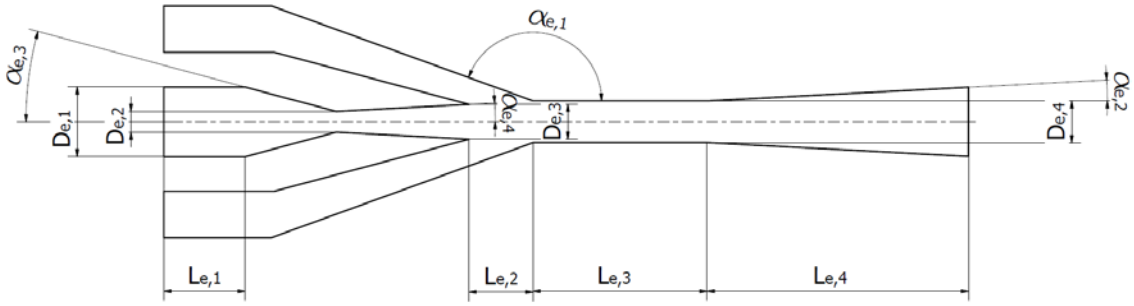


*Figure 6. Schematic illustration of the jet-ejector internal geometry*

| Dimension | | Value | Dimension | | Value |
|---|---|---|---|---|---|
| $\alpha_{e,1}[°]$ | Constant | 160 | $D_{e,3}[mm]$ | Variable | - |
| $\alpha_{e,2}[°]$ | Constant | 3 | $D_{e,4}[mm]$ | Variable | - |
| $\alpha_{e,3}[°]$ | Constant | 15 | $L_{e,1}[mm]$ | Constant | 7 |
| $\alpha_{e,4}[°]$ | Constant | 3 | $L_{e,2}[mm]$ | Variable | - |

| | | | | | |
|---|---|---|---|---|---|
| $D_{e,1}$[mm] | Constant | 6 | $L_{e,3}$[mm] | Constant | 30 |
| $D_{e,2}$[mm] | Variable | - | $L_{e,4}$[mm] | Constant | 45 |

*Table 2. Main dimensions of the jet-ejector*

Those geometric parameters labeled as "Variable", namely, nozzle exit position ($L_{e,2}$), primary nozzle throat diameter ($D_{e.2}$), primary nozzle exit diameter ($D_{e,3}$) and mixing chamber diameter ($D_{e,4}$) are considered as four key geometric parameters [25,26] and they have been varied to maximize the jet-ejector entrainment ratio for each operating condition. In regard to the geometric parameters labeled as "Constant", the diverging angle in the supersonic primary nozzle ($\alpha_{e,4}$) and the diverging angle in the diffuser section ($\alpha_{e,2}$) are reduced to avoid flow detachment. Moreover, the mixing chamber length ($L_{e,3}$) and the diffuser length ($L_{e,4}$) guarantee a uniform flow field across the radial direction. These values are coherent when compared to other research works [27–29].

### 3.2.3 Outdoor conditions and cooling requirements

An evaporating temperature of 13 °C and a condensing temperature of 40 °C have been defined to carry out the CFD simulations. The evaporating temperature is consistent with the typical operating temperatures of air-conditioning applications [20,30]. Considering a pinch point in the heat exchanger of approximately 7 °C the present refrigeration system would meet an indoor temperature of 20 °C. The condensing temperature has been determined assuming an ambient temperature of 31 °C, a pinch point in the condenser of 7 °C and some degree of liquid subcooling. Hence, the JERS is intended to work satisfactorily under relatively adverse outdoor conditions. In fact, the ambient temperature considered is near the maximum daily average temperature in the month of July according to the TMY (see Figure 3).

For each refrigerant under evaluation, the corresponding evaporating/condensing pressure and temperature are shown in Table 3. The primary flow evaporating pressure and, consequently, the primary flow evaporating temperature is not fixed but examined in a parametric study to find its optimum value.

| Refrigerant | Condensing temperature [°C] | Condensing pressure [bar] | Evaporating temperature [°C] | Evaporating pressure [bar] |
|---|---|---|---|---|
| R1234yf | 40 | 10.18 | 13 | 4.80 |
| R1234ze | 40 | 7.67 | 13 | 3.41 |
| R600a | 40 | 5.31 | 13 | 2.43 |

*Table 3. Equivalent condensing and evaporating temperatures for each refrigerant*

## 4. Computational models

This section presents the methodology and the computational models dedicated to estimate the solar collector field and the JERS performance under various operating scenarios. Special emphasis is given to jet-ejector modeling and its validation procedure. Optimization processes of both the jet-ejector internal geometry and the JERS are also discussed in detail.

### 4.1 Solar collector models

The efficiency in the solar collector field side, that is, the capability of the solar collector to transform solar irradiation into thermal power ($\eta_{\mathrm{th-sol}}$), can be determined for different types of collecting devices by using the Hottel-Whillier-Bliss performance curves in a quadratic form (Equation (6)) [8,10,31]:

$$\eta_{\mathrm{th-sol}} = \eta_0 \cdot \left(K_{\theta \mathrm{b}}(\theta) \cdot \frac{G_{\mathrm{b,t}}}{G_{\mathrm{t}}} + K_{\theta \mathrm{d}} \cdot \frac{G_{\mathrm{d,t}}}{G_{\mathrm{t}}}\right) - a_1 \cdot \frac{T_{\mathrm{avg,col}} - T_{\mathrm{amb}}}{G_{\mathrm{t}}} - a_2 \cdot G_{\mathrm{t}} \cdot \left(\frac{T_{\mathrm{avg,col}} - T_{\mathrm{amb}}}{G_{\mathrm{t}}}\right)^2 \quad (6)$$

Where the solar irradiation data (Figure 4) is used to compute the ratio between direct and global solar irradiation $\left(\frac{G_{\mathrm{b,t}}}{G_{\mathrm{t}}}\right)$ as well as the ratio between the diffuse and global solar irradiation $\left(\frac{G_{\mathrm{d,t}}}{G_{\mathrm{t}}}\right)$. Additionally, $\eta_0$ is the zero-loss collector efficiency, $a_1$ is the heat loss coefficient, $a_2$ is the temperature dependence of the heat loss coefficient, $K_{\theta \mathrm{d}}$ is the diffuse incident angle modifier and $K_{\theta \mathrm{b}}$ is the direct incident angle modifier (null angle of incidence assumed $\theta = 0$). The aforementioned fitting coefficients must be adjusted for each particular collector technology and model. Figure 7 represents the dependence

between the solar collector efficiency and the operating temperatures for each model presented in Table 4.

| | $\eta_0[-]$ | $a_1[\mathrm{W}(/\mathrm{m}^2\cdot\mathrm{K})]$ | $a_2[\mathrm{W}/(\mathrm{m}^2\cdot\mathrm{K}^2)]$ | $K_{\theta\mathrm{d}}[-]$ |
|---|---|---|---|---|
| $ETC_{\mathrm{Model-1}}$ | 0.745 | 2.007 | 0.0050 | 0.850 |
| $CPC_{\mathrm{Model-1}}$ | 0.644 | 0.749 | 0.0050 | 0.540 |
| $PTC_{\mathrm{Model-1}}$ | 0.693 | 0.476 | 0.003128 | 0.070 |
| $PTC_{\mathrm{Model-2}}$ | 0.590 | 0.932 | 0 | 0.048 |
| $PTC_{\mathrm{Model-3}}$ | 0.680 | 0.4 | 0.0015 | 0.073 |

*Table 4. Fitting coefficients of performance curves for different collector models. Source:* [8]

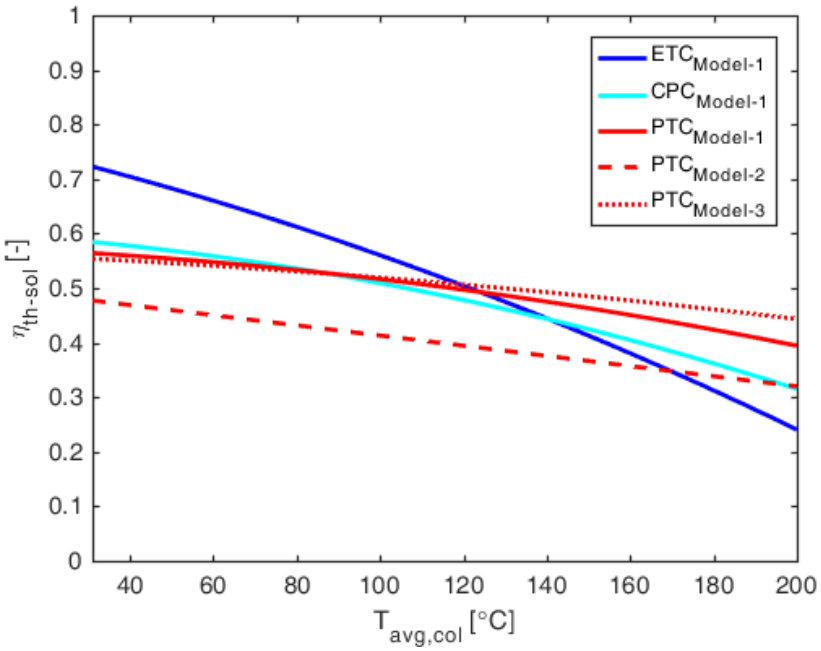


*Figure 7. Solar collector efficiency curves ($G_t = 1000\ W/m^2$ and $T_{amb} = 31°C$)*

## 4.2 Jet-ejector model

### 4.2.1 CFD implementation

The jet-ejector entrainment ratio for each operating condition and geometric configuration has been evaluated by means of CFD simulations. The thermodynamic behavior of the refrigerants under

examination has been modeled by using existing NIST real gas models of R1234yf [32], R1234ze [33] and R600a [34]. Two-dimensional, steady-state and compressible turbulent flow has been assumed as well as single-phase hypothesis. Axisymmetric domain with a quadrilateral structured mesh is selected due to the prevalence of axial flow. The $k-\omega\ SST$ turbulence model which is commonly employed in literature when modelling supersonic flow inside jet-ejectors [35,36] is also assumed together with a pressure-based coupling scheme. Second-order upwind spatial discretization schemes for turbulence and conservation equations are used. The number of cells of the computational domain is around 50,000 in all simulations with slight variations according to the geometric configuration under examination. If the number of cells of the computational domain is further refined (increment from 50,000 cells to 100,000 and 170,000) the relative variation in the entrainment ratio is not exceeding 1%. It must be stressed that slight discrepancies have been found in the magnitude and position of strong shockwaves when the mesh is further refined. Nevertheless, the present CFD approach seeks to predict accurately global flow phenomena parameters i.e, entrainment ratio, rather than making a precise description of local flow phenomena.

Around 330 CFD simulations have been required in the present investigation to find all the optimum jet-ejector geometries. For this reason, the computational economy has special significance.

Total pressure and total temperature boundary conditions have been defined in the jet-ejector primary inlet with 15℃ of superheating to avoid condensation phenomena as the flow expands in the primary nozzle. Following the same reasoning, a superheating temperature of 7℃ has been assumed at the secondary flow inlet.

### 4.2.2 Validation

The CFD approach used in this study has been compared to experimental data available in the literature in order to guarantee that the present CFD model is predicting accurately the jet-ejector entrainment ratio (see Figure 8), which is the key parameter in this investigation to model the jet-ejector performance. The experimental results under consideration are those reported by Hakkaki-Fard et al. [37,38] and García del Valle et al. [28] (geometry “A”) and their study comprises entrainment ratio determination for

different jet-ejector geometries and operating conditions using R134a as working fluid. In the former experimental study the generating pressure ($P_{pf}$) ranges between 29 bar ($T_{\mathrm{sat}} = 84.6\ °C$) and 19.3 bar ($T_{\mathrm{sat}} = 65.9\ °C$), the evaporating pressure ($P_{sf}$) ranges between 2.65 bar ($T_{\mathrm{sat}} = -2.7\ °C$) and 4.15 bar ($T_{\mathrm{sat}} = 10\ °C$) and the condensing pressure ($P_{mf}$) varies between 4.2 bar ($T_{\mathrm{sat}} = 10.4\ °C$) and 8.4 bar ($T_{\mathrm{sat}} = 33°C$). In the present validation process only the operating points in which the jet-ejector operates in the double-chocking mode have been reproduced. In the latter experimental work the generating pressure ($P_{pf}$) is between 25.98 bar ($T_{\mathrm{sat}} = 79.4\ °C$) and 31.9 bar ($T_{\mathrm{sat}} = 89.1\ °C$), the evaporating pressure ($P_{sf}$) varies between 3.49 bar ($T_{\mathrm{sat}} = 5\ °C$) and 4.15 bar ($T_{\mathrm{sat}} = 10\ °C$) and the condensing pressure ($P_{mf}$) changes between 7.47 bar ($T_{\mathrm{sat}} = 28.9\ °C$) and 8.97 bar ($T_{\mathrm{sat}} = 35.4\ °C$).

The evaporating and condensing temperatures of the refrigerants in both the experimental results (R134a) and the numerical approach of the present study (R1234yf, R1234ze and R600a) lead to relatively high operating pressures. Therefore, the real gas effects considered in the CFD setup have special significance [39]. The maximum relative error in the entrainment ratio between the computational and the experimental results is not exceeding 9.3% considering the experimental data of Hakkaki-Fard et al. and 9.5% when compared with the results of García del Valle et al (see Figure 8). Hence, the CFD method is providing reliable estimations of the jet-ejector entrainment ratio.

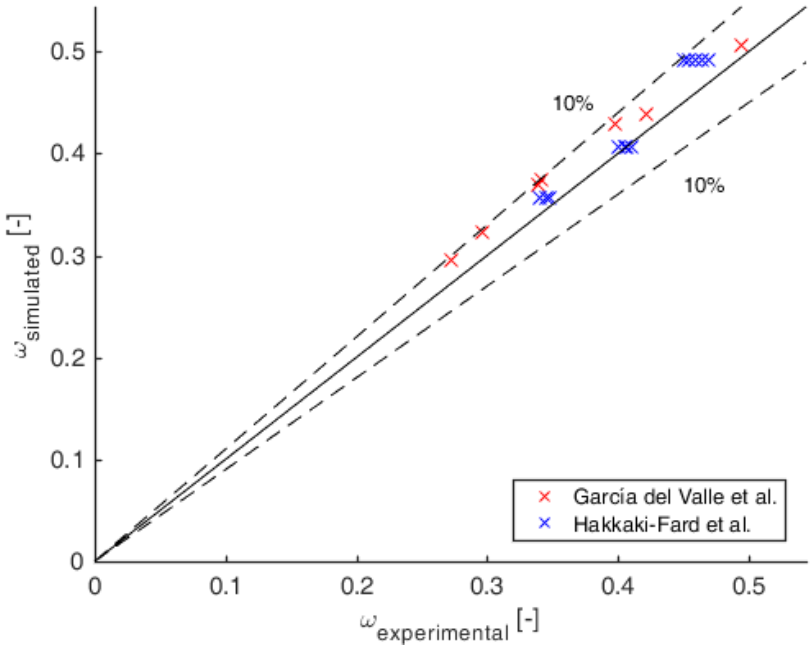


317

318 *Figure 8. Entrainment ratio prediction with the present CFD approach vs experimental data available in*

319 *the literature* [28,37,38]

320

321 ### 4.2.3 Geometric optimization

322

323 The main objective of the jet-ejector optimization process is to obtain the ejector design that maximizes

324 the entrainment ratio for given operating conditions, that is, the condensing and evaporating

325 temperatures specified in Table 3. The decision algorithm when optimizing the jet-ejector internal

326 geometry is represented as the flowchart of Figure 9. The optimization sequence starts after finding a

327 combination of geometric parameters that brings a positive entrainment ratio. This is conducted by using

328 a trial and error method.

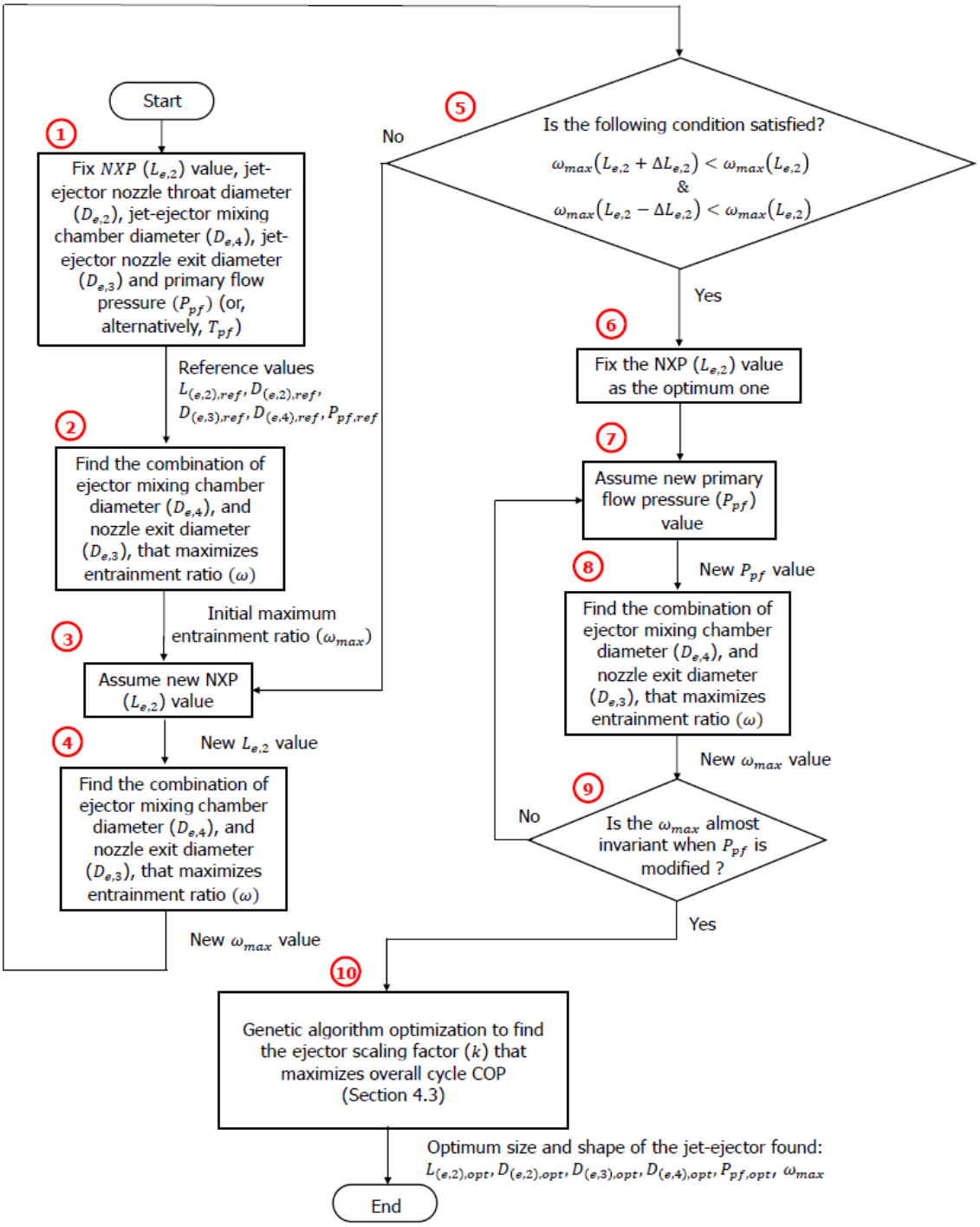


*Figure 9. Optimization sequence to maximize the jet-ejector entrainment ratio (ω)*

## 4.3 JERS governing equations and optimization procedure

The JERS governing equations are feed with the jet-ejector entrainment ratio coming from CFD simulations and are subsequently solved to maximize the power efficiency transformation from thermal energy to cooling capacity $COP_{\mathrm{th}}$. The model of the JERS is based on the conservation of mass and energy in each element of the cycle and it is described elaborately by Galindo et al. [40]. The main assumptions, constraints and objectives are listed below:

**Assumptions**

- Primary and secondary flow expansion processes are modeled by introducing an isentropic efficiency, which is a common approximation in the literature.
- It is supposed that the solar collector field provides 10 kW of thermal power. This hypothesis is assumed just to dimension the jet-ejector component bearing in mind that the whole system might be scaled.
- It is assumed that the primary mass flow rate through the nozzle of the JERS is at choking condition.
- Pressure losses are neglected in all the heat exchangers.
- The expansion valve is assumed to be isenthalpic and the liquid pump is modeled by introducing an isentropic efficiency.
- Subcooling at condenser exit equals to 2°C.

**Objective and resolution strategy**

The objective of the MOGA-II (Multi-Objective Genetic Algorithm) used in the present study is to maximize $COP_{\mathrm{th}}$ by finding the optimum combination of inputs. The multidisciplinary design optimization (MDO) platform modeFrontier has been used as a design tool. The description of the MOGA-II fundamentals implemented in the optimization software can be found in the literature [41–43]. The solving procedure of the governing equations is sequentially displayed in the flowchart of Figure 10. The jet-ejector primary mass flow rate is a priori unknown and it can be computed by using the model proposed by Zegenhagen and Ziegler [39] which includes real gas effects.

It is worth noting that the jet-ejector scaling factor ($k$) and the collector inlet temperature ($T_{\mathrm{in,col}}$) are the input variables of the MOGA-II. The former is intended to modify the size of the reference jet-ejector and, therefore, the primary and secondary mass flow rates passing through this element. The latter is iteratively adjusted to meet the corresponding pinch point in the generator.

$$\dot{m}_{\mathrm{pf}} = \dot{m}_{\mathrm{pf}}(P_{\mathrm{pf}}, T_{\mathrm{pf}}, \mathrm{fluid}, Z, k \cdot D_{(\mathrm{e},2),\mathrm{ref}}) \tag{7}$$

$$\dot{Q}_{\mathrm{ge}} = \dot{m}_{\mathrm{pf}} \cdot (h_{\mathrm{out,ge}}(P_{\mathrm{pf}}, T_{\mathrm{out,ge}}) - h_{\mathrm{in,ge}}(P_{\mathrm{pf}}, T_{\mathrm{in,ge}})) \tag{8}$$

$$\dot{Q}_{\mathrm{ge}} = \dot{m}_{\mathrm{col}} \cdot c_{p,\mathrm{col}} \cdot (T_{\mathrm{out,col}} - T_{\mathrm{in,col}}) \tag{9}$$

$$\dot{Q}_{\mathrm{ev}} = \dot{m}_{\mathrm{sf}} \cdot (h_{\mathrm{out,ev}}(P_{\mathrm{sf}}, T_{\mathrm{out,ev}}) - h_{\mathrm{in,ev}}(P_{\mathrm{sf}}, T_{\mathrm{in,ev}})) \tag{10}$$

$$D_{(\mathrm{e},2),\mathrm{opt}} = k_{\mathrm{opt}} \cdot D_{(\mathrm{e},2),\mathrm{ref}} \tag{11}$$

$$D_{(\mathrm{e},3),\mathrm{opt}} = k_{\mathrm{opt}} \cdot D_{(\mathrm{e},3),\mathrm{ref}} \tag{12}$$

$$D_{(\mathrm{e},4),\mathrm{opt}} = k_{\mathrm{opt}} \cdot D_{(\mathrm{e},4),\mathrm{ref}} \tag{13}$$

$$L_{(\mathrm{e},2),\mathrm{opt}} = k_{\mathrm{opt}} \cdot L_{(\mathrm{e},2),\mathrm{ref}} \tag{14}$$

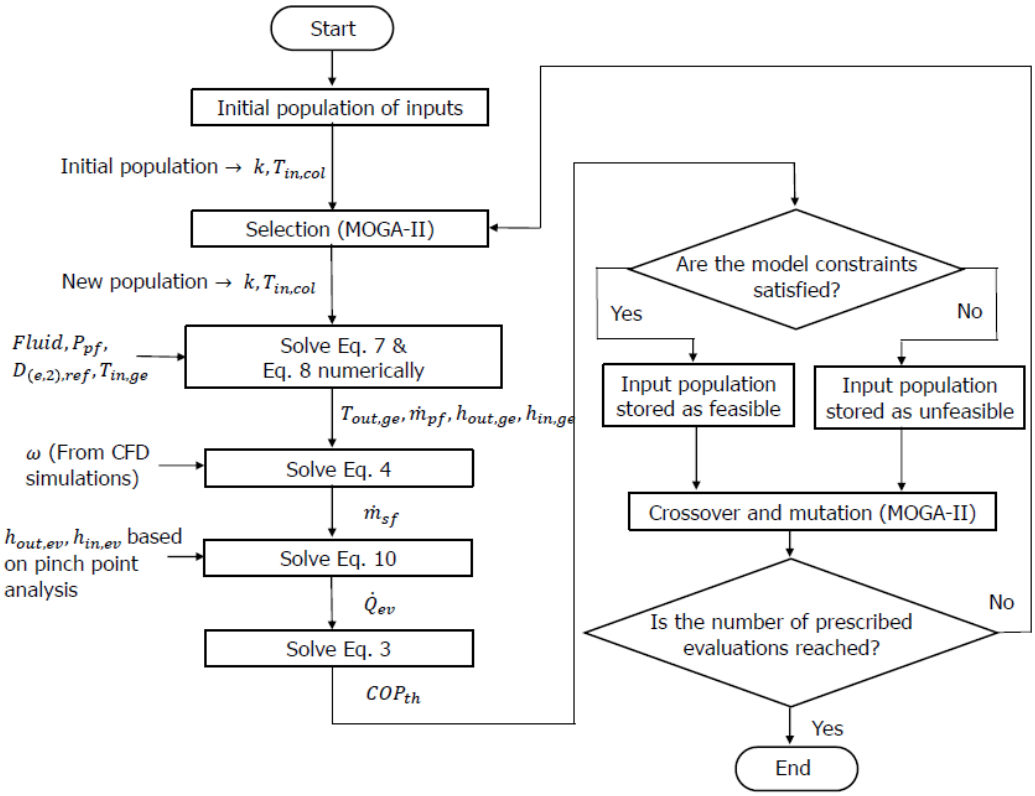


*Figure 10. Resolution flowchart to determine JERS $COP_{th} = \eta_{th,cool}$*

**Constraints**

- Inside the jet-ejector only single-phase flow is permitted to be consistent with the CFD calculations. For this reason, all the MOGA-II solutions showing multiphase flow as primary and secondary flows expand are discarded.
- The pinch point of the heat exchange processes occurring at the evaporator, condenser and generator must be greater than 7°C.

## 5. Results

This section is dedicated to analyze the influence of different refrigerants, operating conditions and solar collector technologies over the system efficiencies, i.e, solar-thermal ($\eta_{\mathrm{th,sol}}$), thermal-cooling ($\eta_{\mathrm{th,cool}}$) and overall ($\eta_{\mathrm{ov}}$) energy conversion processes. Firstly, the jet-ejector geometries that maximized the

entrainment ratio for each operating condition and working fluid are presented. Then, the overall system efficiency is estimated by using the algorithm already introduced in Section 4.3. Subsequently, the refrigerant that provided the best results (maximum $\eta_{ov}$) is selected and the impact of different solar irradiation scenarios and collector types over the system performance is assessed. To conclude, the JERS performance is confronted with a traditional vapor-compression refrigeration system.

## 5.1 Jet-ejector optimization results

Table 5 shows the optimum jet-ejector geometry for each working fluid and generating pressure with the corresponding entrainment ratio. It should be noticed that the scaling factor presented in Equation (7) and Figure 10 is already applied on each jet-ejector dimension according to Equations (11), (12), (13) and (14). To graphically illustrate the jet-ejector entrainment ratio improvement resulting from the optimization process, Figure 11 is provided. The lack of smoothness in some entrainment ratio curves can be attributed to the discretization interval of the geometric dimensions (usually 0.1 mm in the most sensitive geometric parameters) when searching for the optimum geometry. Marginal improvements in entrainment ratio could be achieved if the discretization interval in the optimization process is reduced at the expense of increasing notoriously the number of simulations required to characterize each refrigerant. Hence, this strategy would be not attractive from the computational economy perspective and it does not change the final conclusions of this work.

Figure 11 shows that the generating pressure does not have a decisive influence over the entrainment ratio if the jet-ejector internal geometry is carefully designed. A diminution over the maximum achievable entrainment ratio is found if the generating pressure decreases for a fixed condensing pressure. This trend is maintained regardless of the fluid under consideration. It is also observed that both the primary nozzle area ratio and the jet-ejector area ratio (ratio between mixing chamber area and primary nozzle throat area) tend to increase to counteract the increase of generating pressure in the optimum geometries. These are precisely the most important geometric parameters and must be attentively designed according to the operating conditions. If the optimum geometries for each refrigerant are analyzed under uniform

conditions at the jet-ejector inlet it is observed that the working fluid with the highest specific volume (R600a) presents the smallest jet-ejector throat diameter ($D_{e,2}$) and, consequently, the smallest jet-ejector size, followed by R1234ze and R1234yf.

R600a shows the maximum entrainment ratio ($\omega_{opt} = 0.464$) for $P_{pf} = 31.29$ bar followed by R1234yf ($\omega_{opt} = 0.417$ and $P_{pf} = 35.14$ bar) and R1234ze ($\omega_{opt} = 0.405$ and $P_{pf} = 33.35$ bar). A priori, it is not possible to discern which working fluid is the most convenient in terms of $\eta_{th,cool}$ maximization. For that purpose, the whole refrigeration system must be evaluated.

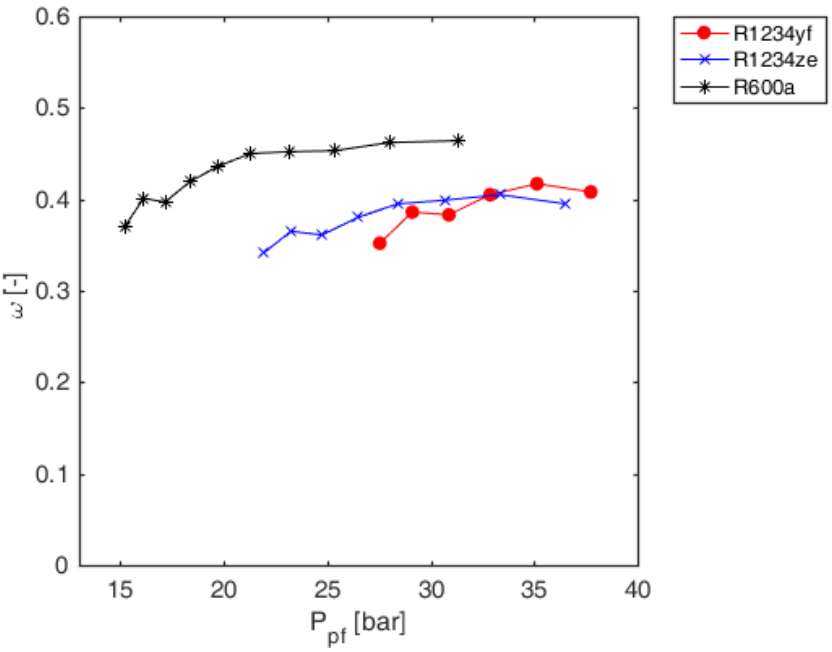


*Figure 11. Optimum jet-ejector entrainment ratio for each primary flow operating pressure*

425

| Working Fluid | $P_{\mathrm{pf}}$[bar] | $P_{\mathrm{sf}}$[bar] | $P_{\mathrm{mf}}$[bar] | $D_{(\mathrm{e},2),\mathrm{opt}}$[mm] | $D_{(\mathrm{e},3),\mathrm{opt}}$[mm] | $D_{(\mathrm{e},4),\mathrm{opt}}$[mm] | $L_{(\mathrm{e},2),\mathrm{opt}}$[mm] | $\omega_{\mathrm{opt}}[-]$ |
|---|---|---|---|---|---|---|---|---|
| R1234yf | 37.74 | 4.80 | 10.19 | 2.14 | 3.33 | 5.46 | 4.16 | 0.408 |
| R1234yf | 35.14 | 4.80 | 10.19 | 2.26 | 3.26 | 5.52 | 4.39 | 0.417 |
| R1234yf | 32.87 | 4.80 | 10.19 | 2.37 | 3.42 | 5.52 | 4.60 | 0.405 |
| R1234yf | 30.88 | 4.80 | 10.19 | 2.47 | 3.43 | 5.48 | 4.80 | 0.383 |
| R1234yf | 29.11 | 4.80 | 10.19 | 2.56 | 3.41 | 5.54 | 4.98 | 0.386 |
| R1234yf | 27.54 | 4.80 | 10.19 | 2.64 | 3.53 | 5.44 | 5.14 | 0.352 |
| R1234ze | 36.52 | 3.41 | 7.67 | 2.05 | 3.42 | 5.93 | 3.99 | 0.395 |
| R1234ze | 33.35 | 3.41 | 7.67 | 2.18 | 3.64 | 5.94 | 4.24 | 0.405 |
| R1234ze | 30.68 | 3.41 | 7.67 | 2.30 | 3.58 | 6.00 | 4.47 | 0.399 |
| R1234ze | 28.41 | 3.41 | 7.67 | 2.41 | 3.74 | 6.01 | 4.68 | 0.395 |
| R1234ze | 26.45 | 3.41 | 7.67 | 2.50 | 3.62 | 5.98 | 4.87 | 0.380 |
| R1234ze | 24.74 | 3.41 | 7.67 | 2.60 | 3.75 | 5.91 | 5.05 | 0.361 |
| R1234ze | 23.24 | 3.41 | 7.67 | 2.69 | 3.58 | 5.82 | 5.23 | 0.365 |
| R1234ze | 21.91 | 3.41 | 7.67 | 2.77 | 3.70 | 5.85 | 5.39 | 0.341 |
| R600a | 31.29 | 2.43 | 5.32 | 1.87 | 3.53 | 5.92 | 3.64 | 0.464 |
| R600a | 28 | 2.43 | 5.32 | 1.99 | 3.54 | 5.97 | 3.87 | 0.462 |
| R600a | 25.33 | 2.43 | 5.32 | 2.10 | 3.50 | 6.07 | 4.08 | 0.453 |
| R600a | 23.13 | 2.43 | 5.32 | 2.21 | 3.68 | 6.00 | 4.29 | 0.452 |
| R600a | 21.28 | 2.43 | 5.32 | 2.31 | 3.59 | 6.03 | 4.49 | 0.450 |
| R600a | 19.70 | 2.43 | 5.32 | 2.41 | 3.48 | 6.02 | 4.68 | 0.436 |
| R600a | 18.34 | 2.43 | 5.32 | 2.50 | 3.62 | 5.98 | 4.87 | 0.419 |
| R600a | 17.16 | 2.43 | 5.32 | 2.60 | 3.75 | 6.01 | 5.05 | 0.397 |
| R600a | 16.12 | 2.43 | 5.32 | 2.69 | 3.58 | 5.97 | 5.23 | 0.401 |
| R600a | 15.20 | 2.43 | 5.32 | 2.77 | 3.39 | 5.86 | 5.39 | 0.370 |

426

427 *Table 5. Optimum jet-ejector geometry for each operating condition and working fluid*

## 5.2 JERS and overall system performance using a parabolic trough collector ($PTC_{\mathbf{Model-3}}$)

One of the parabolic trough collectors, specifically $PTC_{\mathrm{Model-3}}$, has been selected as the reference collector due to its superior operational behavior in a wider range of collector temperatures and solar irradiation conditions when compared to other collector technologies. The sensitivity study has been carried out for a fixed irradiation level (1000 $\mathrm{W/m^2}$) and an ambient temperature of 31°C. Hence, the solar collector efficiency is almost invariant except for the slight differences in collector inlet temperature ($T_{\mathrm{in,col}}$) when the generating pressure varies. The maximum solar irradiation intensity (1000 $\mathrm{W/m^2}$) according to Figure 2 and Figure 3 has been selected to maximize the solar collector performance and thus to evaluate the refrigeration system in the best-case scenario.

Figure 12 depicts the JERS efficiency, the solar collector efficiency and the overall system efficiency against generating pressure for each refrigerant. As specified in the optimization algorithm a detailed jet-ejector geometric optimization has been conducted for each operating pressure and each refrigerant. As the generating pressure increases the JERS efficiency does not exhibit a decreasing trend but it is almost constant. Therefore, this demonstrates that the JERS performance could be marginally enhanced at the expense of a more robust generator capable to withstand higher pressure. It might not be attractive from a cost-benefit criteria because the equipment cost would increase and the efficiency improvement ($\eta_{\mathrm{th,cool}}$) is insignificant. The maximum JERS efficiency corresponds to $\eta_{\mathrm{th,cool}} = 0.377, \eta_{\mathrm{th,cool}} = 0.355, \eta_{\mathrm{th,cool}} = 0.352$ for R1234yf, R600a and R1234ze, respectively. It is noteworthy that the refrigerant with the highest jet-ejector entrainment ratio (R600a) is not the refrigerant with the highest $\eta_{\mathrm{th,cool}}$. This is because more thermal power per unit of cooling demand is required to get superheated vapor at the corresponding generating pressure.

The pump power consumption would be another factor of relevance when evaluating the generating pressure. The power consumption of the liquid pump is far less when compared to the input thermal power of the generator. The power consumption has been determined for the rated thermal power in the

generator (10 kW) and depends on the thermodynamic properties of each working fluid (i.e. the specific volume of each refrigerant, enthalpy variation across the pump…) and the liquid pump pressure ratio. R1234yf shows the greatest power consumption varying between 134W for the lowest operating pressure ($P_{pf} = 27.54\ bar$) and 209W for the highest ($P_{pf} = 37.74\ bar$), followed by R1234ze (85W for $P_{pf} = 21.91\ bar$ and 174W for $P_{pf} = 36.52\ bar$) and R600a (59W for $P_{pf} = 15.20\ bar$ and 146W for $P_{pf} = 31.29\ bar$).

All the refrigerants under consideration offer similar efficiencies when the overall system is assessed. R1234yf maximizes the solar irradiation conversion to cooling power ($\eta_{ov} = 0.201$), closely followed by R1234ze ($\eta_{ov} = 0.187$) and R600a ($\eta_{ov} = 0.184$). This suggests that other criteria should prevail when selecting one of the previous refrigerants for this application (refrigerant or equipment cost, availability, flammability…) rather than the system efficiency.

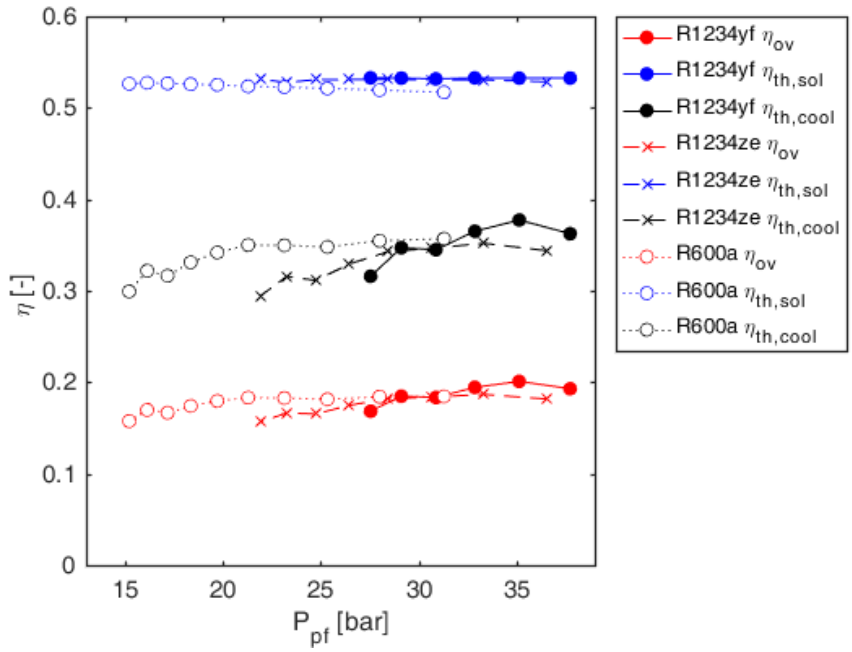


*Figure 12. JERS, solar collector and overall system efficiencies operating with R1234yf, R1234ze and R600a as working fluids ($G_t = 1000\ W/m^2$)*

The present results have been compared with data available in the literature. The aim is to quantify the effectiveness of the optimization procedure introduced in this paper as a way to improve the JERS performance. A rigorous comparison is quite hard because the evaporating and condensing temperatures

considered in the present paper, 13 °$C$ and 40 °$C$, respectively, are not exactly reproduced in the available literature. Nevertheless the $COP_{th}$ results have been compared with some literature data working at similar operating conditions. Bellos and Tzivanidis [10] reported a maximum $COP_{th} = 0.299$ using R141b as working fluid for a condensing temperature of 40 °$C$ and an evaporating temperature of 10 °$C$. Also for the same operating temperatures, Kasperski and Gil [44] reported a maximum $COP_{th} = 0.32$ for R600a. More recently, the same authors calculated a maximum $COP_{th} = 0.23$ [30] keeping the same condensing and evaporating temperatures and considering only non-flammable synthetic refrigerants in the low primary vapor temperature range (below 140 °$C$). Chen et al. [45] obtained a maximum $COP_{th} = 0.38$ and $COP_{th} = 0.25$ for an evaporating temperature of 10 °$C$, and a condensing temperature of 35 °$C$ and 40 °$C$, respectively, when R245fa and R600 are used as refrigerants.

From the previous literature search is not possible to discern whether the superior operational behavior reported in the present paper can be attributed to the higher evaporating temperature or, alternatively, the optimization process and working fluid have an appreciable influence. To elucidate the effect of the optimization process, the operational behavior of the JERS has been compared with literature data of a JERS working under a higher or equal evaporating temperature and a lower condensing temperature, indeed, more beneficial conditions.

Chen et al. [45] performed a screening of working fluids and obtained a $\mathrm{COP_{th}}$ ranging between 0.21 and 0.46 for a condensing temperature of 35°$C$ and an evaporating temperature of 13°$C$. Nehdi et al. [46] reported a $\mathrm{COP_{th}}$ ranging between 0.3 and 0.41 (depending on the working fluid under examination) for an evaporating temperature of 15°$C$ and a condensing temperature of 35°$C$. These values are comparable with the ones indicated in the present study so this would suggest that the thorough optimization of the jet-ejector internal geometry would have a remarkable positive effect over the JERS performance.

## 5.3 Collector type sensitivity analysis

R1234yf has been selected as the reference working fluid for the collector type sensitivity analysis because it maximizes the refrigeration cycle efficiency ($\eta_{\mathrm{th-cool}}$). Hence, the transformation efficiency from

thermal power to cooling power is equal to the optimum value presented in the previous subsection, $\eta_{\mathrm{th,cool}} = 0.377$. To clarify the influence of the solar collector typologies the comparison is carried out for the maximum solar irradiation ($G_{\mathrm{t}} = 1000\ \mathrm{W/m^2}$).

The $ETC_{\mathrm{Model-1}}$ provides the best performance with the peak solar irradiation of 1000 $\mathrm{W/m^2}$ ($\eta_{\mathrm{th,sol}} = 0.565, \eta_{\mathrm{ov}} = 0.213$) as can be seen in Figure 13. In contrast, the worst behavior in the solar collector side is found for the $PTC_{\mathrm{Model-2}}$ ($\eta_{\mathrm{th,sol}} = 0.425$) and it also causes a reduction in the overall system efficiency ($\eta_{\mathrm{ov}} = 0.161$).

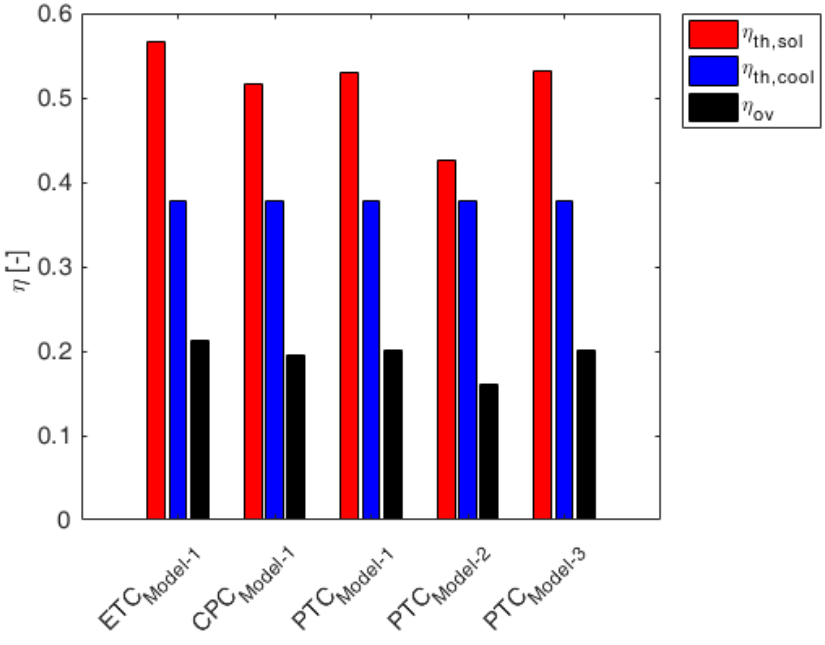


*Figure 13. Influence of the solar collector technology over the system efficiency ($G_t = 1000\ W/m^2$)*

## 5.4 Influence of solar irradiation level

After evaluating the solar collector side for the most favorable irradiation scenario it has special relevance to assess the operational behavior of the solar collector side considering the fluctuating nature of solar irradiation. To do so, the four cases ($C_1 - C_4$) of Table 1 have been studied. According to Figure 14 the

$PTC_{\mathrm{Model-3}}$ presents the most robust behaviour when the solar irradiation changes showing $\eta_{\mathrm{ov}} = 0.201$ when $G_{\mathrm{t}} = 1000\ \mathrm{W/m^2}$ and $\eta_{\mathrm{ov}} = 0.168$ when $G_t = 450\ W/m^2$. On the contrary, $ETC_{Model-1}$ shows the highest deterioration against fluctuating irradiation conditions. Indeed, $\eta_{\mathrm{ov}} = 0.213$ when $G_{\mathrm{t}} = 1000\ \mathrm{W/m^2}$ while $\eta_{\mathrm{ov}} = 0.137$ when $G_{\mathrm{t}} = 450\ \mathrm{W/m^2}$. The performance degradation occurring in the solar field side should be compensated by an increase in the solar collector area to keep invariant the achievable cooling capacity on the JERS side.

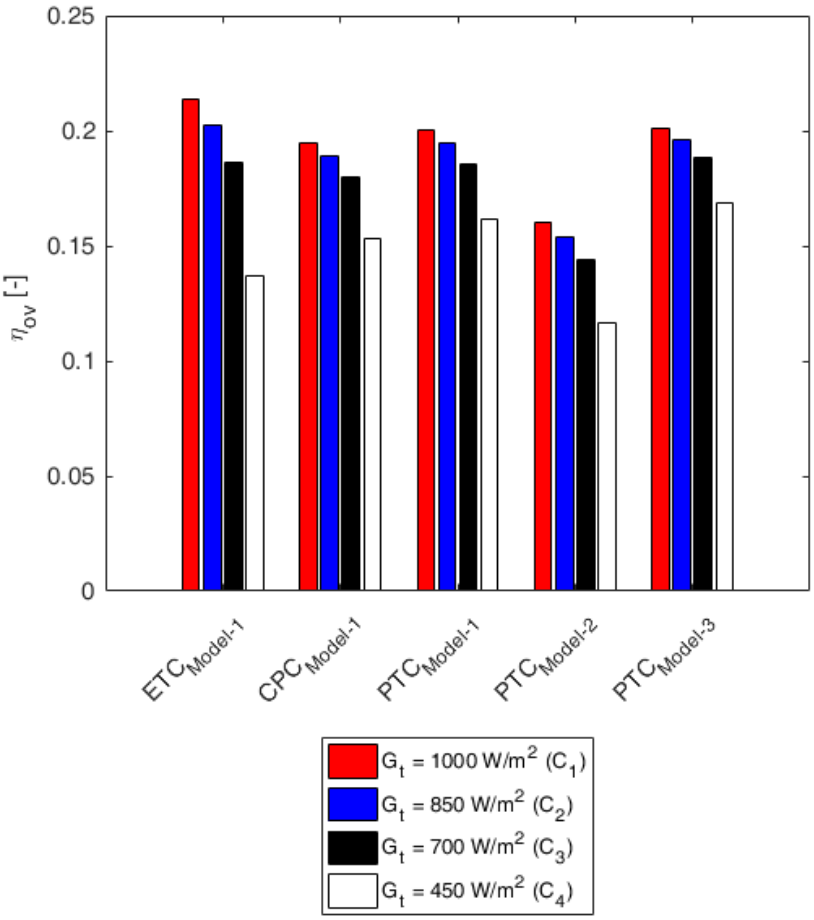


*Figure 14. Influence of different solar irradiation scenarios over system efficiency*

Alternatively, the negative impact over the maximum attainable cooling capacity can be directly related to the diminution in solar irradiation if the solar collector area is fixed. If the solar field is sized for the $PTC_{\mathrm{Model-3}}$ according to the maximum solar irradiation ($G_{\mathrm{t}} = 1000\ \mathrm{W/m^2}$) an efficiency $\eta_{\mathrm{th,sol}} = 0.532$ is obtained for the transformation of solar irradiation to thermal energy. This leads to a collector area of

$18.8\ \mathrm{m}^2$ to meet a thermal capacity of 10 kW in the generator. Figure 15 (left axis) depicts the maximum achievable generator thermal power and cooling capacity as a function of the solar irradiation intensities ($\mathrm{C}_1 - \mathrm{C}_4$) for a fixed collector area. As the solar irradiation is reduced from $1000\ \mathrm{W/m}^2$ ($\mathrm{C}_1$) to $450\ \mathrm{W/m}^2$ ($\mathrm{C}_4$) the cooling capacity and the generator thermal power diminishes by a factor of 2.65. Figure 15 (right axis) represents the jet-ejector primary nozzle size variation that must be accomplished. This characteristic dimension is 1.63 times larger in the case with the peak solar irradiation ($\mathrm{C}_1$) in relation to the case with the lower irradiation intensity ($\mathrm{C}_4$). This reveals the importance of an adjustable jet-ejector to face the fluctuating climatic conditions.

Typically, the daily peak solar irradiation and the peak ambient temperature nearly coincide (normally, a time offset exists) and the daily pattern of solar irradiation and ambient temperature follow a similar trend. The penalty over the maximum achievable cooling capacity caused by the reduction of solar irradiation could be alleviated taking into account that the cooling requirements are partially reduced as the solar irradiation diminishes in a standard summer day because solar irradiation and temperature patterns are almost synchronized. As a first approximation, if the overall heat transfer coefficient and the surface area where the heat transfer takes place remain constant the heat transfer rate is proportional to the difference between indoor and ambient temperature. Figure 16 shows the hourly evolution of $\Delta T$ (left axis), that is, the difference between the mean temperature during the month of July in the TMY (July 2014) and the target indoor temperature together with the solar irradiation pattern of a clear sky day in the same month (right axis). The synchronization between both patterns is envisaged. A priori, the mitigation effect is not sufficient to keep the cooling capacity needs because the temperature difference is $\Delta T = 10°C$ when $G_\mathrm{t} \approx 1000\ \mathrm{W/m}^2$ and $\Delta T = 7.9°C$ when $G_\mathrm{t} \approx 450\ \mathrm{W/m}^2$at $\sim 17{:}00$ (reduction by a factor of 1.26) and $\Delta T = 5.9°C$ when $G_\mathrm{t} \approx 450\ \mathrm{W/m}^2$at $\sim 08{:}00$ (reduction by a factor of 1.69). Indeed, the cooling capacity is reduced by a factor of 2.65 in these hours as mentioned above.

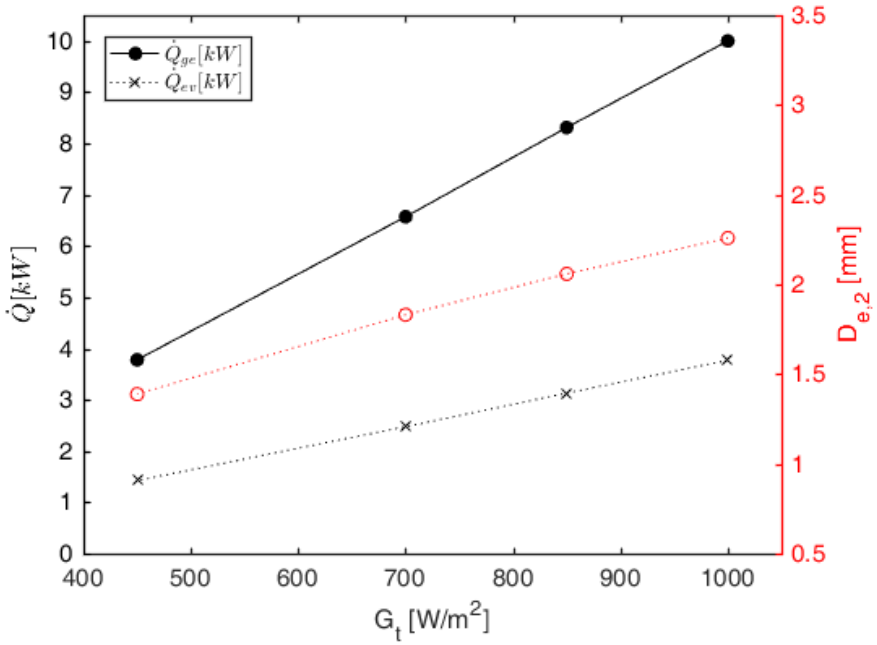


551

552 *Figure 15. Maximum achievable thermal power and cooling capacity according to the solar irradiation (left*

553 *axis). Required primary nozzle throat diameter to work satisfactorily in different solar irradiation scenarios*

554 *(right axis).*

555

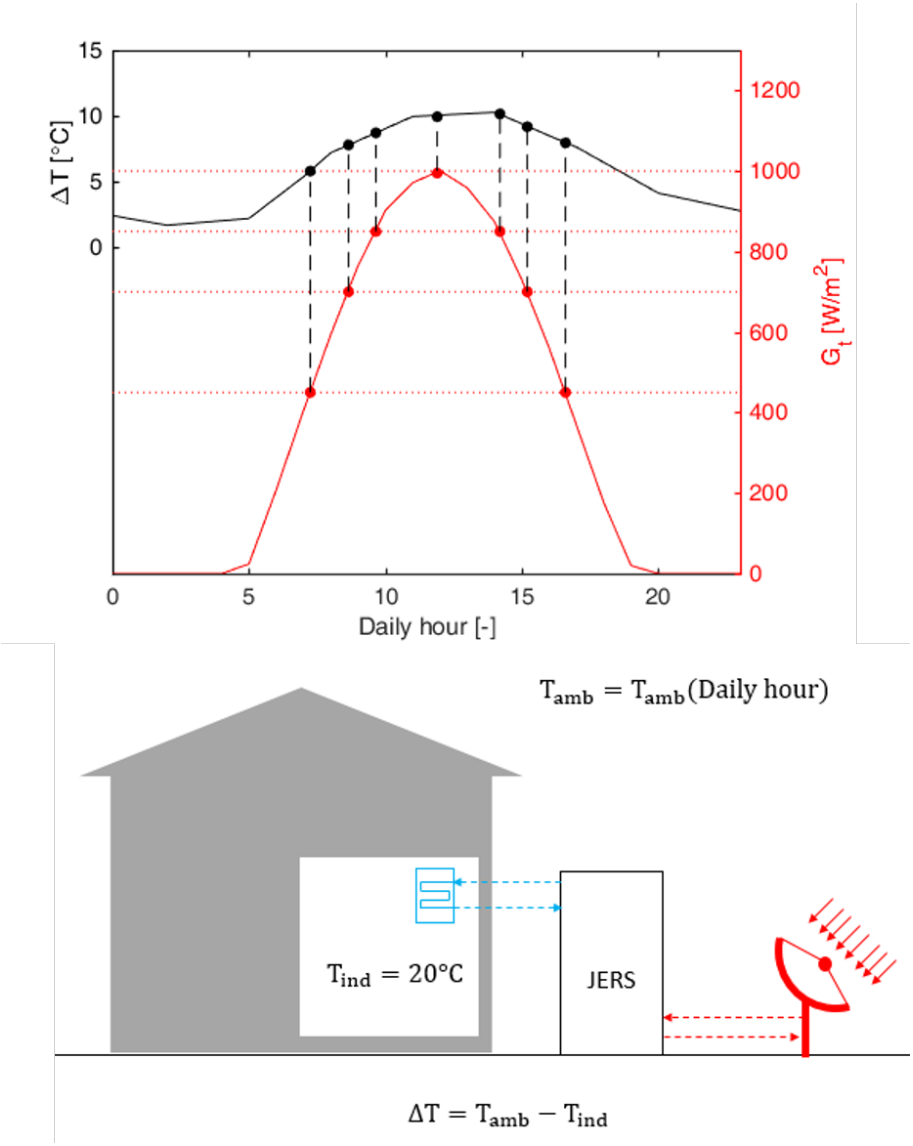


556

557 *Figure 16. Difference between the outdoor and indoor temperature for the solar irradiation scenarios*

558 *assessed.*

559

560 ## 5.5 Comparison with a traditional vapor-compression air-conditioning system

561

562 In view of the previous results, the design efforts focused on improving the jet-ejector behavior by

563 optimizing its internal shape are essential to improve the overall system performance. The relatively low

564 energy conversion efficiency can be attributed to the JERS itself as well as the solar collector field but the

565 JERS still has the greatest improvement potential. This translates into a relatively high collector area per

unit of cooling power and, consequently, in higher investment cost. Nonetheless, if the input power to drive the JERS operating in its peak efficiency scenario (R1234yf as refrigerant and $\eta_{\mathrm{th,cool}} = 0.377$) is compared with a traditional vapor-compression system working under the same cooling requirements and outdoor conditions (assuming also the same degree of liquid subcooling in the condenser and vapor superheating in the evaporator) it is found that the power consumption of the traditional system is 2.52 times higher than the JERS. It is worthy emphasizing that the main power input in the JERS and the conventional refrigeration system corresponds to the liquid pump and the compressor, respectively. Both elements have been modeled in this comparison assuming an isentropic efficiency ($\eta_{\mathrm{comp}} = \eta_{\mathrm{pm}} = 0.85$). Equivalently, the efficiency improvement with respect to the conventional vapor-compression system can be evaluated by means of the traditional COP definition. In such a case $COP_{\mathrm{h}} = \dot{Q}_{\mathrm{ev}}/\dot{W}_{\mathrm{comp}} = 7.74$ for the traditional system and $COP_{\mathrm{h}} = \dot{Q}_{\mathrm{ev}}/\dot{W}_{\mathrm{pm}} = 19.51$ for the JERS. In view of the above, hybrid configurations in which the JERS would be intended to assist a vapor-compression refrigeration machine with the aim of reducing the compressor's power consumption could be promising alternatives from the perspective of both power efficiency and investment cost.

## 6. Conclusions

The present paper evaluates numerically a solar-driven jet-ejector refrigeration system using environmentally friendly and new generation refrigerants with low ecological impact, namely, R1234yf, R1234ze and R600a. A detailed jet-ejector shape optimization is carried out in each operating condition as a mechanism to improve the overall cycle performance. The influence of variable solar irradiation conditions and different collector technologies over the overall system performance is also evaluated. The main conclusions are outlined below:

- Considering slight variations, the primary flow pressure does not affect significantly the jet-ejector entrainment ratio and the maximum achievable $\eta_{\mathrm{th,cool}}$ if the jet-ejector internal geometry (primary nozzle throat and exit diameter, NXP and mixing chamber diameter) is thoroughly designed according to the operating conditions. Bearing this in mind the jet-ejector

refrigeration system achieves a maximum $\eta_{\mathrm{th,cool}} = 0.377$ for R1234yf, closely followed by R600a and R1234ze.

- If the analysis is extended to the overall system, that is, the coupling of the jet-ejector refrigeration system and solar collector field it is observed that R1234yf refrigerant offered the best performance in terms of solar irradiation transformation to cooling capacity ($\eta_{\mathrm{ov}} = 0.201$) closely followed by the system operating with R1234ze ($\eta_{\mathrm{ov}} = 0.187$) and R600a ($\eta_{\mathrm{ov}} = 0.184$). Hence, if the jet-ejector internal geometry is carefully designed, the overall system performance is almost insensitive to the working fluids under examination.

- The ETC (Evacuated Tube Collector) model under consideration maximizes the overall system efficiency for the peak solar irradiation (1000 $\mathrm{W/m^2}$) but one of the PTC (Parabolic Trough Collectors) offers the best performance in those situations with fluctuant solar irradiation.

- The power consumption of a traditional vapor-compression system working under the same cooling requirements and outdoor conditions is 2.52 times higher than the JERS.

**Acknowledgements**

Authors want to acknowledge to the institution "Conselleria d´Educació, Investigació, Cultura i Esport de la Generalitat Valenciana" and its grant program "Subvenciones para la contratación de personal investigador de carácter predoctoral" for doctoral studies (ACIF/2018/124).

## 7. References

[1] Balaras CA, Grossman G, Henning HM, Infante Ferreira CA, Podesser E, Wang L, et al. Solar air conditioning in Europe-an overview. Renew Sustain Energy Rev 2007;11:299–314. doi:10.1016/j.rser.2005.02.003.

[2] Kim DS, Infante Ferreira CA. Solar refrigeration options - a state-of-the-art review. Int J Refrig 2008;31:3–15. doi:10.1016/j.ijrefrig.2007.07.011.

[3] Kalkan N, Young EA, Celiktas A. Solar thermal air conditioning technology reducing the footprint

of solar thermal air conditioning. Renew Sustain Energy Rev 2012;16:6352–83. doi:10.1016/j.rser.2012.07.014.

[4] Weber C, Berger M, Mehling F, Heinrich A, Núñez T. Solar cooling with water-ammonia absorption chillers and concentrating solar collector - Operational experience. Int J Refrig 2014;39:57–76. doi:10.1016/j.ijrefrig.2013.08.022.

[5] Xu SM, Huang XD, Du R. An investigation of the solar powered absorption refrigeration system with advanced energy storage technology. Sol Energy 2011;85:1794–804. doi:10.1016/j.solener.2011.04.022.

[6] Ketfi O, Merzouk M, Merzouk NK, Metenani S El. Performance of a Single Effect Solar Absorption Cooling System (Libr-H2O). Energy Procedia 2015;74:130–8. doi:10.1016/j.egypro.2015.07.534.

[7] Chekirou W, Boukheit N, Karaali A. Performance improvement of adsorption solar cooling system. Int J Hydrogen Energy 2016;41:7169–74. doi:10.1016/j.ijhydene.2016.02.140.

[8] Cabrera FJ, Fernández-García A, Silva RMP, Pérez-García M. Use of parabolic trough solar collectors for solar refrigeration and air-conditioning applications. Renew Sustain Energy Rev 2013;20:103–18. doi:10.1016/j.rser.2012.11.081.

[9] Huang BJ, Chang JM, Petrenko VA, Zhuk KB. A solar ejector cooling system using refrigerant R141b. Sol Energy 1998;64:223–6. doi:10.1016/S0038-092X(98)00082-6.

[10] Bellos E, Tzivanidis C. Optimum design of a solar ejector refrigeration system for various operating scenarios. Energy Convers Manag 2017;154:11–24. doi:10.1016/j.enconman.2017.10.057.

[11] Chen J, Jarall S, Havtun H, Palm B. A review on versatile ejector applications in refrigeration systems. Renew Sustain Energy Rev 2015;49:67–90. doi:10.1016/j.rser.2015.04.073.

[12] Pollerberg C, Ali AHH, Dötsch C. Solar driven steam jet ejector chiller. Appl Therm Eng 2009;29:1245–52. doi:10.1016/j.applthermaleng.2008.06.017.

[13] Varga S, Oliveira AC, Palmero-Marrero A, Vrba J. Preliminary experimental results with a solar driven ejector air conditioner in Portugal. Renew Energy 2017;109:83–92. doi:10.1016/j.renene.2017.03.016.

[14] Tashtoush B, Alshare A, Al-Rifai S. Hourly dynamic simulation of solar ejector cooling system using TRNSYS for Jordanian climate. Energy Convers Manag 2015;100:288–99. doi:10.1016/j.enconman.2015.05.010.

[15] Pollerberg C, Heinzel A, Weidner E. Model of a solar driven steam jet ejector chiller and investigation of its dynamic operational behaviour. Sol Energy 2009;83:732–42. doi:10.1016/j.solener.2008.11.003.

[16] Zhang T, Mohamed S. Conceptual Design and Analysis of Hydrocarbon-Based Solar Thermal Power and Ejector Cooling Systems in Hot Climates. J Sol Energy Eng 2014;137. doi:10.1115/1.4028365.

[17] Tashtoush B, Alshare A, Al-Rifai S. Performance study of ejector cooling cycle at critical mode under superheated primary flow. Energy Convers Manag 2015;94:300–10. doi:10.1016/j.enconman.2015.01.039.

[18] Pereira PR, Varga S, Soares J, Oliveira AC, Lopes AM, De Almeida FG, et al. Experimental results with a variable geometry ejector using R600a as working fluid. Int J Refrig 2014;46:77–85. doi:10.1016/j.ijrefrig.2014.06.016.

[19] Yen RH, Huang BJ, Chen CY, Shiu TY, Cheng CW, Chen SS, et al. Performance optimization for a variable throat ejector in a solar refrigeration system. Int J Refrig 2013;36:1512–20. doi:10.1016/j.ijrefrig.2013.04.005.

[20] Varga S, Lebre PMS, Oliveira AC. CFD study of a variable area ratio ejector using R600a and

669 R152a refrigerants. Int J Refrig 2013;36:157–65. doi:10.1016/j.ijrefrig.2012.10.016.

670 [21] Allouche Y, Bouden C, Varga S. A CFD analysis of the flow structure inside a steam ejector to
671 identify the suitable experimental operating conditions for a solar-driven refrigeration system.
672 Int J Refrig 2014;39:186–95. doi:10.1016/j.ijrefrig.2013.07.027.

673 [22] European Commission Joint Research Centre (JRC). PVGIS n.d.
674 http://re.jrc.ec.europa.eu/pvgis.html (accessed January 21, 2020).

675 [23] Kalogirou SA. Solar thermal collectors and applications. vol. 30. 2004.
676 doi:10.1016/j.pecs.2004.02.001.

677 [24] Belessiotis V, Kalogirou S, Delyannis E, Belessiotis V, Kalogirou S, Delyannis E. Indirect Solar
678 Desalination (MSF, MED, MVC, TVC). Therm Sol Desalin 2016:283–326. doi:10.1016/B978-0-12-
679 809656-7.00006-4.

680 [25] Ruangtrakoon N, Aphornratana S, Sriveerakul T. Experimental studies of a steam jet refrigeration
681 cycle: Effect of the primary nozzle geometries to system performance. Exp Therm Fluid Sci
682 2011;35:676–83. doi:10.1016/j.expthermflusci.2011.01.001.

683 [26] Varga S, Oliveira AC, Diaconu B. Influence of geometrical factors on steam ejector performance -
684 A numerical assessment. Int J Refrig 2009;32:1694–701. doi:10.1016/j.ijrefrig.2009.05.009.

685 [27] Shestopalov KO, Huang BJ, Petrenko VO, Volovyk OS. Investigation of an experimental ejector
686 refrigeration machine operating with refrigerant R245fa at design and off-design working
687 conditions. Part 2. Theoretical and experimental results. Int J Refrig 2015;55:212–23.
688 doi:10.1016/j.ijrefrig.2015.02.004.

689 [28] García Del Valle J, Saíz Jabardo JM, Castro Ruiz F, San José Alonso JF. An experimental
690 investigation of a R-134a ejector refrigeration system. Int J Refrig 2014;46:105–13.
691 doi:10.1016/j.ijrefrig.2014.05.028.

692 [29] Chen Z, Jin X, Shimizu A, Hihara E, Dang C. Effects of the nozzle configuration on solar-powered
693 variable geometry ejectors. Sol Energy 2017;150:275–86. doi:10.1016/j.solener.2017.04.017.

694 [30] Gil B, Kasperski J. Efficiency analysis of alternative refrigerants for ejector cooling cycles. Energy
695 Convers Manag 2015;94:12–8. doi:10.1016/j.enconman.2015.01.056.

696 [31] Shirazi A, Taylor RA, White SD, Morrison GL. A systematic parametric study and feasibility
697 assessment of solar-assisted single-effect, double-effect, and triple-effect absorption chillers for
698 heating and cooling applications. Energy Convers Manag 2016;114:258–77.
699 doi:10.1016/j.enconman.2016.01.070.

700 [32] Richter M, McLinden MO, Lemmon EW. Thermodynamic properties of 2,3,3,3-tetrafluoroprop-1-
701 ene (R1234yf): Vapor pressure and p - ϕ - T Measurements and an Equation of State. J Chem Eng
702 Data 2011;56:3254–64. doi:10.1021/je200369m.

703 [33] Mclinden MJO, Thol M, Lemmon EW. Thermodynamic Properties of Measurements of Density
704 and Vapor Pressure and a Comprehensive Equation of State. Int Refrig Air Cond Conf 2010.

705 [34] Bücker D, Wagner W. Reference equations of state for the thermodynamic properties of fluid
706 phase n-butane and isobutane. J Phys Chem Ref Data 2006;35:929–1019.
707 doi:10.1063/1.1901687.

708 [35] Croquer S, Poncet S, Aidoun Z. Turbulence modeling of a single-phase R134a supersonic ejector.
709 Part 1: Numerical benchmark. Int J Refrig 2016;61:140–52. doi:10.1016/j.ijrefrig.2015.07.030.

710 [36] Kolář J, Dvořák V. Verification of K-ω SST Turbulence Model for Supersonic Internal Flows.
711 WasetOrg 2011;5:262–6.

712 [37] Hakkaki-Fard A, Aidoun Z, Ouzzane M. A computational methodology for ejector design and
713 performance maximisation. Energy Convers Manag 2015;105:1291–302.
714 doi:10.1016/j.enconman.2015.08.070.

[38] Hakkaki-Fard A, Poirier M, Aidoun Z, Ouzzane M, Giguère D. An experimental study of ejectors supported by CFD. Refrig Sci Technol 2015:2030–7. doi:10.18462/iir.icr.2015.0609.

[39] Zegenhagen MT, Ziegler F. A one-dimensional model of a jet-ejector in critical double choking operation with R134a as a refrigerant including real gas effects. Int J Refrig 2015;55:72–84. doi:10.1016/j.ijrefrig.2015.03.013.

[40] Galindo J, Dolz V, Tiseira A, Ponce-Mora A. Thermodynamic Analysis and Optimization of a Jet Ejector Refrigeration Cycle Used To Cool Down the Intake Air in an Ic Engine. Int J Refrig 2019;103:253–63. doi:10.1016/j.ijrefrig.2019.04.019.

[41] Poloni C, Pediroda V. GA coupled with computationally expensive simulations: tools to improve efficiency. In: Quagliarella D, Périaux J, Poloni C, Winter G, editors. Genet. Algorithms Evol. Strateg. Eng. Comput. Sci. Recent Adv. Ind. Appl., John Wiley & Sons; 1998, p. 267–88.

[42] Aittokoski T, Miettinen K. Efficient evolutionary approach to approximate the Pareto-optimal set in multiobjective optimization, UPS-EMOA. Optim Methods Softw 2010;25:841–58. doi:10.1080/10556780903548265.

[43] Poles S. MOGA-II An improved Multi-Objective Genetic Algorithm. ModeFRONTIER User Man 2003:16.

[44] Kasperski J, Gil B. Performance estimation of ejector cycles using heavier hydrocarbon refrigerants. Appl Therm Eng 2014;71:197–203. doi:10.1016/j.applthermaleng.2014.06.057.

[45] Chen J, Havtun H, Palm B. Screening of working fluids for the ejector refrigeration system. Int J Refrig 2014;47:1–14. doi:10.1016/j.ijrefrig.2014.07.016.

[46] Nehdi E, Kairouani L, Elakhdar M. A solar ejector air-conditioning system using environment-friendly working fluids. Int J Energy Res 2008;32:1194–201. doi:10.1002/er.1413.